Understanding fast macroscale fracture from microcrack post mortem patterns

Claudia Guerra[a,b], Julien Scheibert[a,c,d,e,1], Daniel Bonamy[a], and Davy Dalmas[c]

[a]Commissariat à l'Energie Atomique, Saclay Institute of Matter and Radiation, Service de Physique et Chimie des Surfaces et Interfaces, Group Complex Systems and Fracture, F-91191 Gif sur Yvette, France; [b]Facultad de Ingeniería Mecánica y Eléctrica, Universidad Autónoma de Nuevo León, Avenida Universidad, San Nicolás, Ciudad Universitaria, C.P. 66450, San Nicolás de los Garza, Nuevo León, Mexico; [c]Unité Mixte Centre National de la Recherche Scientifique/Saint-Gobain, Surface du Verre et Interfaces, 39 Quai Lucien Lefranc, 93303 Aubervilliers Cedex, France; [d]Physics of Geological Processes, University of Oslo, P.O. Box 1048 Blindern, N-0316 Oslo, Norway; and [e]Laboratoire de Tribologie et Dynamique des Systèmes, Centre National de la Recherche Scientifique, Ecole Centrale de Lyon, 36 Avenue Guy de Collongue, F-69134 Ecully cedex, France

Edited by L. B. Freund, University of Illinois at Urbana-Champaign, Urbana, IL, and approved November 28, 2011 (received for review August 11, 2011)

Dynamic crack propagation drives catastrophic solid failures. In many amorphous brittle materials, sufficiently fast crack growth involves small-scale, high-frequency microcracking damage localized near the crack tip. The ultrafast dynamics of microcrack nucleation, growth, and coalescence is inaccessible experimentally and fast crack propagation was therefore studied only as a macroscale average. Here, we overcome this limitation in polymethylmethacrylate, the archetype of brittle amorphous materials: We reconstruct the complete spatiotemporal microcracking dynamics, with micrometer/nanosecond resolution, through post mortem analysis of the fracture surfaces. We find that all individual microcracks propagate at the same low, load-independent velocity. Collectively, the main effect of microcracks is not to slow down fracture by increasing the energy required for crack propagation, as commonly believed, but on the contrary to boost the macroscale velocity through an acceleration factor selected on geometric grounds. Our results emphasize the key role of damage-related internal variables in the selection of macroscale fracture dynamics.

dynamic fracture | crack speed | polymeric glass | fracture energy | fracture process

The fracture of brittle amorphous materials is usually described using the linear elastic fracture mechanics (LEFM) framework (1–4), which considers the straight propagation of a single smooth crack. All dissipative processes (e.g., plastic deformation or bond breaking) are assumed to be localized in a small zone around the crack tip (fracture process zone, FPZ). Crack velocity, v, is then predicted from the balance between the flux of mechanical energy released from the surrounding elastic material into the FPZ (5) and the dissipation rate within this zone. The former is computable within continuum theory and connects to the stress intensity factor, K, which describes the macroscopic forcing applied on the crack tip and depends on the external loading and specimen geometry only. The dissipation rate is quantified by the fracture energy, Γ, required to expose a new unit area of cracked surfaces, to be measured experimentally. The resulting equation of motion reads (1) $\Gamma \approx (1 - v/c_R)K^2/E$, where E and c_R denote the material's Young's modulus and Rayleigh wave speed, respectively.

Polymethylmethacrylate (PMMA) is often considered as the archetype of nominally brittle materials and, therefore, has been one of the most widely used materials against which theories have been confronted from the early stages of fracture mechanics. Yet, in PMMA, single smooth cracks are actually observed for slow propagation only. Fast enough cracks ($v > v_a \sim 0.2\, c_R$; ref. 6) propagate through the nucleation, growth, and coalescence, in the fracture plane, of individual microcracks (6–9). Cracks faster than $v_b \sim 0.4\, c_R$ also involve aborted out-of-plane secondary cracks known as microbranches (2, 10, 11), which prevent LEFM from being applicable (11). LEFM has been shown to agree with experiments as long as no microbranch is involved (6, 11–13)—i.e., even in the presence of microcracks, provided a suitable velocity dependence of the fracture energy, $\Gamma(v)$, is prescribed (6, 11).

Recent experiments using PMMA (see ref. 6, *Materials and Methods*, and Fig. S1) showed that, above v_a, the slope of $\Gamma(v)$ drops (6) (see Fig. 1), suggesting that microcracks make macroscale cracks dissipate less or/and propagate faster than a single crack would. These possible conclusions are at odds with the common view that damage through opening mode microcracks slows down crack propagation by increasing energy dissipation (3, 7, 14). Understanding this counterintuitive behavior requires unraveling the coupling between (*i*) the space-time dynamics of damage at the FPZ scale and (*ii*) the crack dynamics at the macroscale. The time interval between two successive microcrack nucleation events is typically a few tens of nanoseconds. Such a timescale makes real-time local measurements of microcracking dynamics beyond current researchers' reach. Hence, fast crack propagation has been studied only through measurements of the average dynamics of the macroscopic crack front (5–16).

Quantitative fractography is an appealing tool to probe microscale damage mechanisms. Fracture surfaces are indeed known to record fracture processes down to the nanoscale (9, 17). In particular, in many materials including PMMA (Fig. 2*A*), microcracks leave characteristic conic-like markings on fracture surfaces (3, 6–9). These patterns are commonly understood through a geometrical model first developed in ref. 18 and improved in, e.g., refs. 7 and 19. In this model, each conic-like marking corresponds to the intersection of two penny-shaped microcracks, nucleated at point-like nucleation centers and growing at speeds c_1 and c_2 along two slightly different planes (Fig. 2*B* and Fig. S2). The numerical implementation of this model demonstrated that microcracking is responsible for some of the complexity of macroscopic crack growth (7) (e.g., mist fracture surfaces decorated by conic-like markings and strong fluctuations in the velocity signal, $v(t)$). However, the agreement remained only qualitative because simplifying prescriptions were used for the characteristics of microcracking dynamics (7), namely (*i*) the location of nucleation centers, (*ii*) c_2/c_1, and (*iii*) the nucleation criterion.

Experimental Determination of the Dynamics of Individual Microcracks

Here, we determine experimentally the microscopic rules for the nucleation and growth of microcracks, by analyzing the morphology of each individual conic-like marking on different millimeter-sized fracture surfaces (see, e.g., Fig. 2*A*) corresponding to different K (i.e., to different v in the range 0.23–0.49 c_R) (*Materials and Methods*). We first find that, irrespective of K, the spatial distribution of nucleation centers is Poissonian (see Fig. 3*A*, *Upper*

Author contributions: C.G., J.S., D.B., and D.D. designed research, performed research, analyzed data, and wrote the paper.

The authors declare no conflict of interest.

This article is a PNAS Direct Submission.

[1]To whom correspondence should be addressed. E-mail: julien.scheibert@ec-lyon.fr.

This article contains supporting information online at www.pnas.org/lookup/suppl/doi:10.1073/pnas.1113205109/-/DCSupplemental.

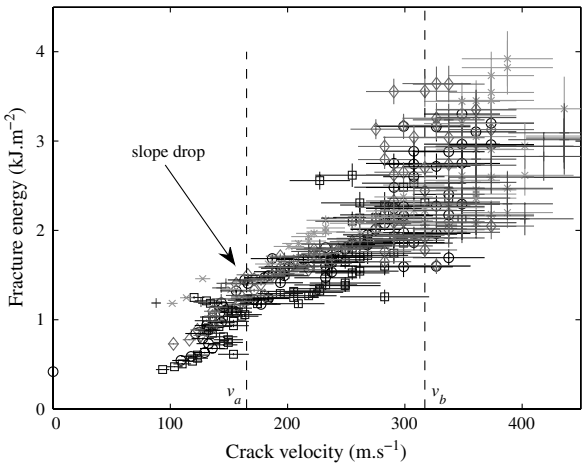

Fig. 1. Fracture energy Γ as a function of macroscale crack velocity v (adapted from ref. 6). Different symbols correspond to different experiments. The two vertical dashed lines correspond to v_a (microcracking onset) and v_b (microbranching onset). Below v_b, all the experimental points collapse onto a single $\Gamma(v)$ curve. The slope of this curve exhibits a drop at v_a.

and Fig. S3) (i.e., the centers are homogeneously and randomly distributed in space, without correlation). Such a distribution is consistent with the usual view that microcracks nucleate at some preexisting weak defects randomly distributed within the material's volume, when a crack tip running in their vicinity sufficiently enhances the stress field (3, 9). The increase in mean surface density of nucleation centers, ρ, with K (Fig. 3*A*, *Lower*) is attributed to the increase in FPZ size with K, which yields more volume defects turning into microcracks (6) (see *SI Text*). Because ρ completely characterizes Poisson distributions, it will be used hereafter as the parameter as a function of which the various quantities will be plotted.

Stationarity of macroscopic crack propagation at the scale of each millimetric-sized image requires the ratio c_2/c_1 of the velocities of two successive microcracks to be one, on average.

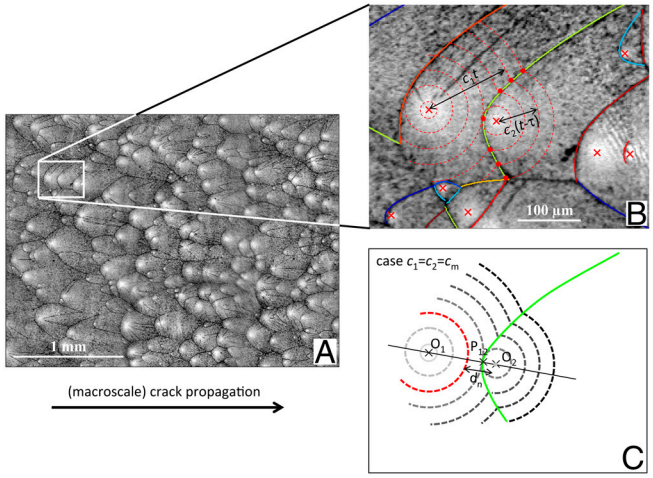

Fig. 2. Fractographic signature of microcracking in the dynamic fracture of PMMA. (*A*) Typical fractographic microscope image ($K \simeq 3.10 \pm 0.05$ MPa·m$^{1/2}$). Bright regions correspond to microcrack nucleation centers (*Materials and Methods*). (*B*) Red dashed circle arcs sketch successive front locations of two interacting microcracks (nucleated at $t = 0$ and $t = \tau$) growing radially at speeds c_1 and c_2. Fitting of fractographic branches (color lines) with a geometrical model (Eq. S1) allows measuring c_2/c_1. (*C*) When $c_2 = c_1$, markings (green line) are conic branches (Eq. S2), and the distance d_n between the triggered microcrack center and the triggering front at the nucleation time $t = \tau$ (highlighted in red) is twice the apex-to-focus distance, O_2P_{12}.

A smaller (larger) value would indeed produce a decelerating (accelerating) macroscale crack. This requirement has consequences on the geometry of conic-like markings (see *SI Text* and Fig. S2), which were checked: We fitted all individual markings with the shape predicted using the geometrical model (see Fig. 2*B* and *SI Text*), with c_2/c_1 being the only adjustable parameter. Irrespective of ρ, c_2/c_1 is found equal to one within 4% standard deviation (see Fig. 3*B* and Fig. S4). In the following, we will neglect the slight dispersion of c_2/c_1 and consider that, for any given ρ, all microcracks propagate at the same velocity: $c_2 = c_1 = c_m$, where c_m denotes the speed of individual microcracks and a priori depends on the macroscopic external loading K (or equivalently on ρ).

In these conditions, the intersection between two microcracks is a true conic. Its focus coincides with the nucleation center of the triggered microcrack, and the apex-to-focus distance is half the distance d_n between the triggering front and the triggered center at the instant of nucleation (see Fig. 2*C* and *SI Text*). Hence, d_n defines the nucleation criterion. Its cumulative distribution is well fitted by a two-parameters parabolic function, irrespective of ρ (Fig. 3*C*, *Upper* and Fig. S5). Variations of the mean value $\bar{d}_n$ with ρ exhibit two regimes: an initial linear increase followed by a saturating plateau, when ρ exceeds a value ρ_{sat} (Fig. 3*C*, *Lower*). The linear behavior comes from the fact that d_n and ρ both scale linearly with the FPZ size (see *SI Text*). The transition is understood as the point where $\bar{d}_n$ becomes comparable with the mean distance between nucleation centers (see *SI Text* and Fig. S6).

Deterministic Reconstruction of the Microcracking Damage History

The analyses performed up to now permit a full characterization of the statistics of microcrack nucleation, growth, and coalescence within the FPZ. To unravel how this FPZ quantitatively operates to relate the macroscale crack velocity, v, to the microscale velocity, c_m, of individual microcracks, we feed the geometrical model with the observed locations of all individual nucleation centers and the corresponding distances at nucleation, d_n. We then simulate the space-time evolution of the fracturing process with the constraint that all microcracks propagate at the same velocity $c_1 = c_2 = c_m$ (*Materials and Methods*). Note that, at this point, c_m is constant within the FPZ but can depend on K (or equivalently on ρ). Fig. 4 *A* and *B* shows typical snapshots of the simulated crack dynamics (see Movies S1 and S2). Apart from edge effects (see *SI Text* and Fig. S7), the matching between the experimental conics and the simulated ones is quite satisfactory (Fig. 4 *C* and *D*) for all values of ρ. As expected, the simulated dynamics thus provide a deterministic reconstruction of the ultrafast microcracking dynamics. The spatial resolution of approximately 2 µm (pixel size) and the time resolution of approximately 10 ns (pixel size divided by c_m, demonstrated hereafter to be a load-independent constant close to a value $c_m \sim 200$ m/s) are much beyond standard experimental mechanics methods like acoustic emission or fast imaging. Similar deterministic nucleation and geometrical growth models are used in a broad range of fields including metallurgy (20), biology (21), and superconductivity (22).

Macroscale Crack Dynamics

To shed light on the macroscale effect of microcracking damage, we now focus on the time evolution of the average location of the simulated crack front (Fig. 5*A*). For each ρ, this evolution is linear, meaning that the average front has a constant velocity, $A \times c_m$, the value of which was found insensitive to edge effects (see *SI Text* and Fig. S7). Fig. 5*B* shows that the acceleration factor A equals one only for $\rho = 0$, and then increases with ρ. The time evolution of the position of a single point of the front (Fig. 5*A*) sheds light on the origin of this effective acceleration. The point motion is jerky, with sudden jumps corresponding to

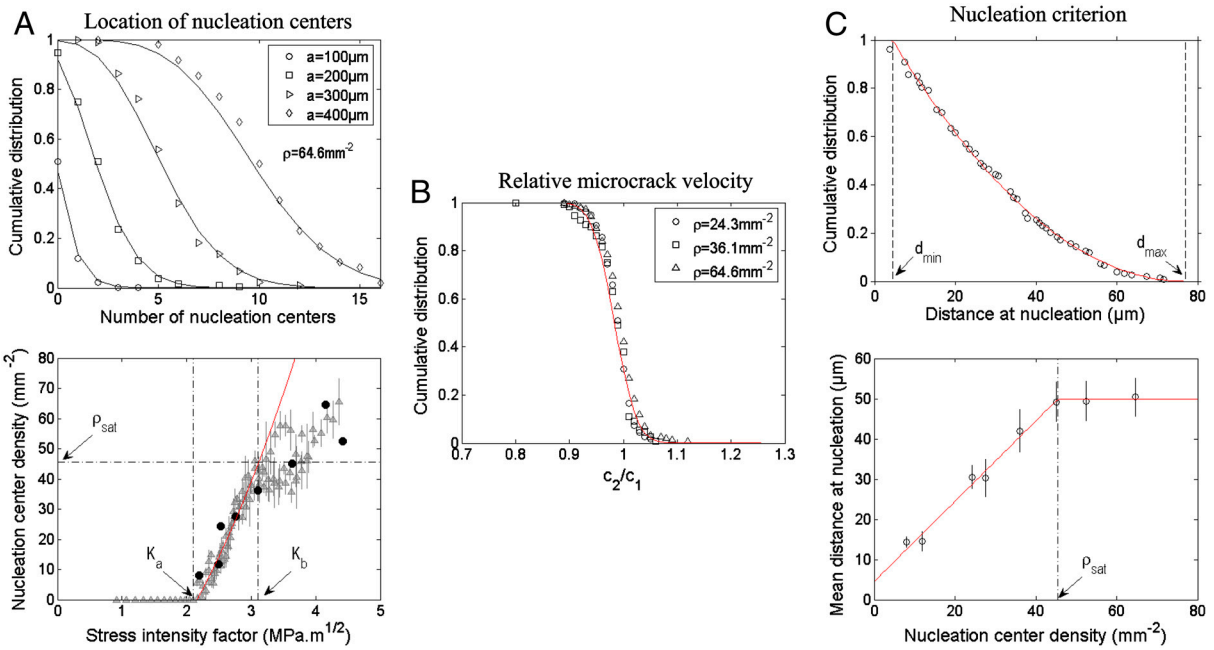

Fig. 3. Microcrack dynamics deduced from fracture surfaces. (*A*, *Upper*) Cumulative distributions for the number of nucleation centers in square regions of size a, for $K \simeq 4.15 \pm 0.07$ MPa·m$^{1/2}$. Solid lines: Poisson function with parameter ρa^2. The fitting parameter ρ is a independent, indicating homogeneous uncorrelated random distribution with mean surface density ρ. Similar results hold for all K (Fig. S3). (*Lower*) Black discs indicate $\rho(K)$ curve superimposed to that obtained from the data reported in ref. 6 (gray triangles, vertical lines indicate standard deviation). Red line: fit using Eq. **S3** in the range $K_a = 2.1$ MPa·m$^{1/2}$ < $K < K_b = 3.1$ MPa·m$^{1/2}$ (see *SI Text*). $\rho_{sat} \simeq 45.5$ mm^{-2}. (*B*) Cumulative distribution, for various ρ, of the velocity ratio c_2/c_1 obtained via fitting fractographic branches using the geometrical model (see Eq. **S1** and *SI Text*). Red line: Fitted normal distribution (average 0.98 and standard deviation 0.03). Similar results hold for each ρ (Fig. S4). (*C*, *Upper*) Cumulative distribution of d_n for $\rho = 27.5$ mm^{-2}. Red line: best two-parameters fit $P(d_n) = [(d_{max} - d_n)/(d_{max} - d_{min})]^2$. Here $d_{min} = 4$ μm, $d_{max} = 77$ μm. Similar fits hold for all ρ (Fig. S5). (*Lower*) Mean distance at nucleation $\bar{d}_n$ as a function of ρ. Error bars: ±one standard deviation. Red line: fit using Eq. **S4** up to a saturating value $\bar{d}_n \simeq 50$ μm reached at ρ_{sat} (see *SI Text*).

microcrack coalescence events, and the velocity between jumps is close to c_m. Hence, as the rate of coalescence events increases with ρ, A also increases with ρ. A simple mean-field lattice model, which evaluates the rate of coalescence events, yields (see *SI Text* and Fig. S8)

$$A = \frac{1}{1 - b\bar{d}_n\sqrt{\rho}}, \qquad [1]$$

where b is a numerical factor $\simeq 1$. This equation, when combined with the observed evolution of $\bar{d}_n$ with ρ (Fig. 3*C*, *Lower*, red line),

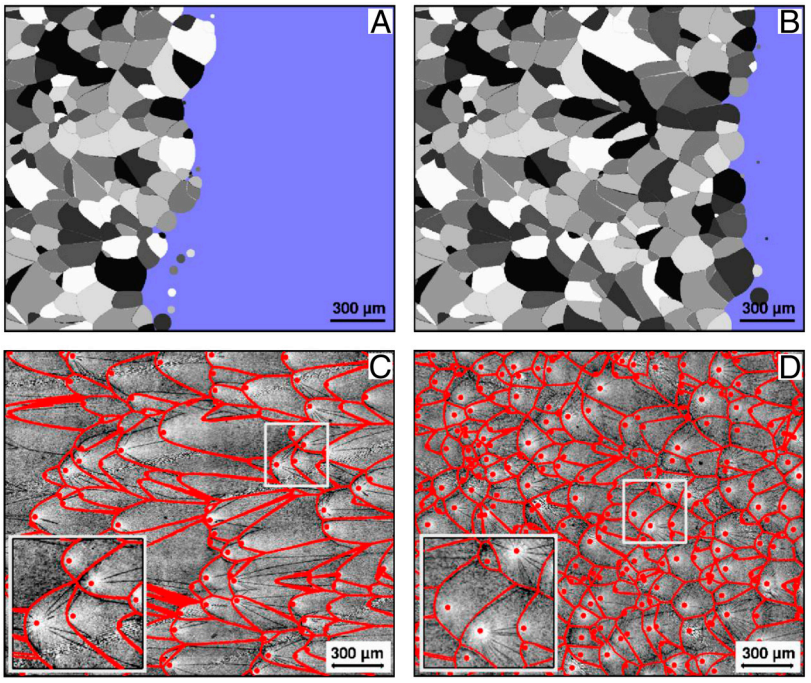

Fig. 4. Deterministic reconstruction of microscale damage and fracture processes. (*A* and *B*) Successive snapshots of the reconstructed crack propagation and associated conic markings for $\rho = 64.6$ mm^{-2}. Crack propagates from left to right. (*C* and *D*) Fracture surface images (gray level) for (*C*) $\rho = 27.5$ mm^{-2} ($K \simeq 2.77$ MPa·m$^{1/2}$) and (*D*) $\rho = 64.6$ mm^{-2} ($K \simeq 4.18$ MPa·m$^{1/2}$) compared to the reconstructed conic markings (red lines). Red dots indicate nucleation centers.

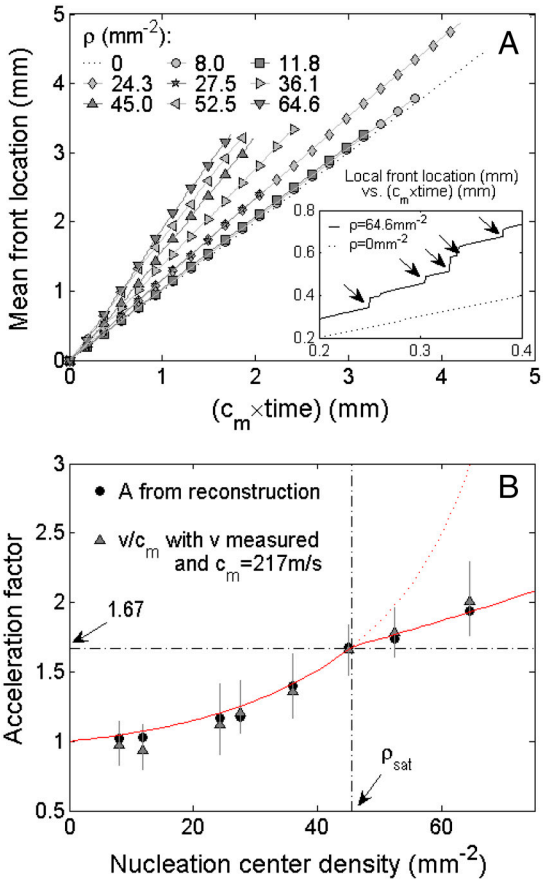

Fig. 5. From slow microcracks to fast collective macroscopic crack motion. (*A*) Time evolution (scaled by c_m) of the average location of the simulated crack front for various ρ. The fitted slopes of these curves define the acceleration factor *A*. $A = 1$ for $\rho = 0$. (*Inset*) Evolution of the location of a single point of the simulated front, for $\rho = 64.6$ mm^2, together with that expected for $\rho = 0$ (slope 1). Jumps correspond to coalescence events with microcracks. Between jumps, the slope is close to one. (*B*) Black dots: Evolution of the reconstructed acceleration factor *A* as a function of ρ. Triangles: Ratio of the measured macroscopic crack speed, *v*, over the microscopic velocity fitted to be $c_m = 217 \pm 3$ m/s. Error bars indicate the minimum and maximum measured velocities within the considered fractographic image. Thick red line: Eq. **1** with $b = 1.19 \pm 0.02$. A change in regime occurs for $\rho = \rho_{sat}$ (vertical dashed line), which corresponds to a velocity of 1.67 c_m (horizontal dashed line). ±stands for 95% confidence interval.

gives the red line in Fig. 5*B*, which is in very good agreement with reconstructed velocities.

The question remains of the possible dependence of c_m with ρ. Fig. 5*B* shows that, if we chose a ρ-independent $c_m = 217 \pm 3$ m/s $= 0.24 \pm 0.01$ c_R, the ρ dependence of the reconstructed acceleration factor A is identical to the ratio of the measured macroscopic crack speed, v, over c_m. This matching means that the propagation speed of microcracks is not only identical for two successive microcracks, but also all along the crack path, irrespective of ρ—and hence of K. Note that c_m is found very close to the maximum speed, $\simeq$204 m/s or $\simeq$0.23 c_R, of individual crack fronts in PMMA originating from the fracture energy increase with FPZ size (6). The change in the ρ dependence of A observed at ρ_{sat} in Fig. 5*B* corresponds to a macroscopic crack speed $\simeq 1.67$ c_m $\simeq 0.41$ c_R. This velocity is very close to the onset of the microbranching instability (0.36 c_R in PMMA; ref. 11), which suggests that this instability could be related to the steric effect responsible for the saturation of $\bar{d}_n(\rho)$ above ρ_{sat}.

Discussion

In dynamic fracture, the relationship between the opening force and the speed at which a macroscopic crack moves forward is controlled by dissipative and nonlinear processes that develop at the microscale within the FPZ. The space and timescales associated with the FPZ dynamics are usually too small to enable a real-time and space monitoring of these processes. Here, we demonstrate that such a detailed monitoring is actually possible in PMMA, the archetype of nominally brittle materials, by analyzing post mortem the patterns left on fracture surfaces by microcracking damage.

Our results show that, in PMMA, the true local propagation speed of single cracks is limited to a fairly low value c_m, about 0.23 c_R, although the apparent speed, v, measured at the continuum-level scale, can be much higher. When $v \geq c_m$, the macroscopic crack is actually found to progress through the coalescence of microcracks, all growing at the same constant velocity c_m. The main effect of microcracking damage, therefore, is not, as commonly believed (3, 7, 14), to slow down fracture by increasing the energy required to further propagate a crack, but on the contrary to boost the macroscopic (group) crack velocity to a value larger than what would have been obtained in their absence.

We conjecture that the limiting value c_m of the local crack speed is set by the material-dependent dissipative and nonlinear processes that develop in the highly stressed/strained zones in the very vicinity of the (micro)crack tips, like, e.g., thermal (23), viscoelastic (15, 24), or hyperelastic (5, 25) processes. As for the subsequent boost from c_m to the continuum-level scale velocity v, it is shown here to take the form of a purely geometric factor controlled by two microscopic quantities: (*i*) The density of nucleation centers ρ and (*ii*) the mean distance at nucleation $\bar{d}_n$. These two internal variables characterize the damaging state and evolve with the amount of mechanical energy flowing into the FPZ. As such, they are material-dependent functions of the external loading K, the knowledge of which permits to fully relate v and c_m.

This enhanced description of dynamic brittle fracture, demonstrated on PMMA, can likely be extended qualitatively to all materials involving propagation-triggered microcracks, e.g., oxide glass (3, 26), polymeric glasses (3, 9), polycrystals (3), rocks (27, 28), and bones (29). Further work is required to check this conjecture, and subsequently to quantitatively determine how c_m, ρ, and $\bar{d}_n$ are selected in these materials. From the geometric nature of the acceleration factor, we also anticipate that fast macroscopic cracks in other fracture modes could similarly originate from the collective motion of many slow microcracks.

Materials and Methods

Experiments. Fracture surfaces were obtained from the experiments described in ref. 6. Dynamic cracks were driven in PMMA (Young's modulus $E = 2.8$ GPa and Poisson's ratio $\nu = 0.36$, yielding a Rayleigh wave speed $c_R = 880$ m/s) using the wedge-splitting geometry sketched in Fig. S1. Specimens were prepared from parallelepipeds of size $140 \times 125 \times 15$ mm^3 in the propagation, loading, and thickness directions, respectively. Subsequently, a notch was formed (*i*) by cutting a 25×25 mm^2 rectangle from the middle of one of the 125×15 mm^2 edges; and (*ii*) by subsequently adding a 10-mm groove deeper into the specimen. A circular hole with a radius ranging between 2 and 8 mm was eventually drilled at the tip of the groove. Two steel jaws equipped with rollers were placed on both sides of the rectangular cutout and a steel wedge of semiangle 15° was pushed between them at constant velocity 38 m/s up to crack initiation. Crack speed was measured using a modified version of the potential drop technique: A series of 90 parallel conductive lines (2.4-nm-thick Cr layer covered with 23-nm-thick Au layer), 0.5-mm wide with a period of 1 mm (space accuracy 40 μm) were deposited on one of the two 140×125 mm^2 sides of the specimen, connected in parallel and alimented with a voltage source. As the crack propagated, the lines were cut at successive times detected with an oscilloscope (time accuracy 0.1 μs) and allowed to record the instantaneous macroscopic crack velocity v, with better than 10% accuracy. The variations of the quasi-static stress intensity factor K were computed using 2D finite element calculations (software

CASTEM 2007) on the exact experimental geometry, assuming plane stress conditions, and a constant wedge position throughout failure of the specimen. Values for the fracture energy Γ were directly obtained from the equation of motion $\Gamma \approx (1 - v/c_R)K^2/E$ by combining the v measurements and the K calculations.

Post Mortem Analysis. Post mortem topography images were obtained with an optical profilometer (M3D; Fogale Nanotech, ×5 objective yielding square pixels of size 1.86 μm) at various locations along the fracture surfaces in different broken specimens—each zone of observation is characterized by a given value of K. For each location, nine neighboring images were gathered to provide an observation field of at least 2×2 mm^2, large enough to carry out statistical analyses. The presence of a highly reflective area at the focus of each conic-like marking results from plastic deformations at microcrack nucleation and allows locating unambiguously all nucleation centers (see Fig. 2*A*). For many microcracks, fragmentation lines focusing on the nucleation center were also observed, and they helped increase the accuracy of the location. For each marking, we made an initial guess about which microcrack triggered its nucleation. The apex of the marking was defined as the intersection between the segment linking the triggering and triggered centers and the conic-like marking. A new guess was made if the simulated marking did not resemble the observed one.

Simulation. The macroscopic crack front was initially straight, vertical, and located on the left of the image. It started propagating toward the right at constant velocity (one pixel per time step). When the macroscopic crack front reached a distance d_n from the closest nucleation center, a microcrack was nucleated and made to grow radially at the same velocity. The total front was then made of both the initially straight translating front and the newly created radially growing circular front. When these two coincided, propagation was continued in the unbroken part of the specimen only. Intersection points defined the conic-like marking. The same procedure was applied each time the shortest distance between the total front and another nucleation center was found to have decreased down to the distance at nucleation d_n associated with this center. Edge effects were minimized in the evaluation of A by considering only the times after all points of the initial front coalesced with a nucleated microcrack, and before the first point of the total front reached the right edge of the image.

ACKNOWLEDGMENTS. We thank A. Prevost for his help with the profilometry measurements. We thank K. Ravi-Chandar for helpful discussions. We thank L. Barbier, G. Debrégeas, A. Malthe-Sorenssen, J. Mathiesen, K.J. Måloy, P. Meakin, and C. Rountree for careful reading of the manuscript. We acknowledge funding from French Agence Nationale de la Recherche through Grant ANR-05-JCJC-0088, from Triangle de la Physique through Grant 2007-46, from Mexican Consejo Nacional de Ciencia y Tecnología through Grant 190091, and from the European Union through Marie Curie Grant PIEF-GA-2009-237089. This work was supported by a Center of Excellence Grant to Physics of Geological Processes from the Norwegian Research Council.

1. Freund LB (1990) *Dynamic Fracture Mechanics* (Cambridge Univ Press, Cambridge, England), pp 367–441.
2. Fineberg J, Marder M (1999) Instability in dynamic fracture. *Phys Rep* 313:1–108.
3. Ravi-Chandar K (2004) *Dynamic Fracture* (Elsevier, Amsterdam), pp 189–216.
4. Cox B, Gao HJ, Gross D, Rittel D (2005) Modern topics and challenges in dynamic fracture. *J Mech Phys Solids* 53:565–596.
5. Livne A, Bouchbinder E, Svetlizky I, Fineberg J (2010) The near-tip fields of fast cracks. *Science* 327:1359–1363.
6. Scheibert J, Guerra C, Célarié F, Dalmas D, Bonamy D (2010) Brittle-quasibrittle transition in dynamic fracture: An energetic signature. *Phys Rev Lett* 104:045501.
7. Ravi-Chandar K, Yang B (1997) On the role of microcracks in the dynamic fracture of brittle materials. *J Mech Phys Solids* 45:535–563.
8. Ravi-Chandar K (1998) Dynamic fracture of nominally brittle materials. *Int J Fract* 90:83–102.
9. Hull D (1999) *Fractography: Observing, Measuring and Interpreting Fracture Surface Topography* (Cambridge Univ Press, Cambridge, England), pp 121–156.
10. Sharon E, Gross SP, Fineberg J (1995) Local crack branching as a mechanism for instability in dynamic fracture. *Phys Rev Lett* 74:5096–5099.
11. Sharon E, Fineberg J (1999) Confirming the continuum theory of dynamic brittle fracture for fast cracks. *Nature* 397:333–335.
12. Bergkvist H (1974) Some experiments on crack motion and arrest in polymethylmethacrylate. *Eng Fract Mech* 6:621–622.
13. Goldman T, Livne A, Fineberg J (2010) Acquisition of inertia by a moving crack. *Phys Rev Lett* 104:114301.
14. Washabaugh PD, Knauss WG (1994) A Reconciliation of dynamic crack velocity and Rayleigh-wave speed in isotropic brittle solids. *Int J Fract* 65:97–114.
15. Boudet JF, Ciliberto S, Steinberg V (1996) Dynamics of crack propagation in brittle materials. *J Phys II* 6:1493–1516.
16. Rosakis AJ, Samudrala O, Coker D (1999) Cracks faster than the shear wave speed. *Science* 284:1337–1340.
17. Kermode JR, et al. (2008) Low-speed fracture instabilities in a brittle crystal. *Nature* 455:1224–1227.
18. Smekal A (1953) On the fracturing processes underlying the brittle behavior of materials under uniaxial and multiaxial loading (Translated from German). *Oesterr Ing Arch* 7:49–70.
19. Rabinovitch A, Belizovsky G, Bahat D (2000) Origin of mist and hackle patterns in brittle fracture. *Phys Rev B Condens Matter Mater Phys* 61:14968.
20. Mukhopadhyay P, Loeck M, Gottstein G (2007) A cellular operator model for the simulation of static recrystallization. *Acta Mater* 55:551–564.
21. Jettestuen E, Nermoen A, Hestmark G, Timdal E, Mathiesen J (2010) Competition on the rocks: Community growth and tessellation. *PLoS One* 5:e12820.
22. Vestgarden JI, Shantsev DV, Galperin YM, Johansen TH (2008) Flux distribution in superconducting films with holes. *Phys Rev B Condens Matter Mater Phys* 77:014521.
23. Estevez R, Tijssens MGA, Van der Giessen E (2000) Modeling of the competition between shear yielding and crazing in glassy polymers. *J Mech Phys Solids* 48:2585–2617.
24. Persson BNJ, Brener EA (2005) Crack propagation in viscoelastic solids. *Phys Rev E Stat Nonlin Soft Matter Phys* 71:036123.
25. Buehler MJ, Abraham FF, Gao HJ (2003) Hyperelasticity governs dynamic fracture at a critical length scale. *Nature* 426:141–146.
26. Rountree CL, et al. (2002) Atomistic aspects of crack propagation in brittle materials: Multimillion atom molecular dynamics simulations. *Annu Rev Mater Res* 32:377–400.
27. Moore DE, Lockner DA (1995) The role of microcracking in shear-fracture propagation in granite. *J Struct Geol* 17:95–114.
28. Kobchenko M, et al. (2011) 4D imaging of fracturing in organic-rich shales during heating. *J Geophys Res* 116:B12201.
29. Nalla RK, Kinney JH, Ritchie RO (2003) Mechanistic fracture criteria for the failure of human cortical bone. *Nat Mater* 2:164–168.